Journal of Materials Chemistry C

CoMnCrGa: A Novel Ferromagnetic Material with High Spin-Polarization for Room Temperature Spintronics

Journal:	*Journal of Materials Chemistry C*
Manuscript ID	TC-ART-08-2023-002813.R2
Article Type:	Paper
Date Submitted by the Author:	13-Oct-2023
Complete List of Authors:	Gupta, Shuvankar; Saha Institute of Nuclear Physics, Condensed Matter Physics Chakraborty, Sudip; Saha Institute of Nuclear Physics, Condensed Matter Physics Bhasin, Vidha; Bhabha Atomic Research Centre, Pakhira, Santanu; Ames Laboratory, ; Karlsruhe Institute of Technology, Dan, Shovan; TIFR, Condensed Matter Physics and Materials Science; Barreteau, Celine; Institut de Chimie et des Materiaux Paris-Est Crivello, Jean-Claude; Institut de Chimie et des Materiaux Paris-Est Jha, Shambhu; Bhabha Atomic Research Centre, Trombay, Applied Spectroscopy Division Avdeev, Maxim; Australian Nuclear Science and Technology Organisation (ANSTO), Australian Centre for Neutron Scattering Dibyendu, B.; Bhabha Atomic Research Centre, Paul-Boncour, Valérie; Université Paris-Est, Institut de Chimie et des Matériaux Paris-Est, UMR 7182 CNRS UPEC, 2 rue H. Dunant, 94320 Thiais, France Mazumdar, Chandan; Saha Institute of Nuclear Physics, Condensed Matter Physics Division

Journal Name

ARTICLE TYPE

Cite this: DOI: 00.0000/xxxxxxxxxx

CoMnCrGa: A Novel Ferromagnetic Material with High Spin-Polarization for Room Temperature Spintronics†

Shuvankar Gupta[a], Sudip Chakraborty[a], Vidha Bhasin[b], Santanu Pakhira[c], Shovan Dan[d], Celine Barreteau[e], Jean-Claude Crivello[e], S.N. Jha[f], Maxim Avdeev[g,h], D. Bhattacharyya[b], V. Paul-Boncour[e], and Chandan Mazumdar[a,*]

Received Date
Accepted Date

DOI: 00.0000/xxxxxxxxxx

Here, we report synthesis of a novel quaternary Heusler alloy CoMnCrGa and its structural, magnetic, transport and electronic properties using both experimental and theoretical methods. DFT calculations on ordered crystal structure with specific atomic positions (Ga at 4*a*, Mn at 4*b*, Cr at 4*c* and Co at 4*d*) reveals a half-metallic ferromagnetic (HMF) ground state having a very high spin polarization of 96.1%. In this work we show that despite having a mix of Mn (4*b*) and Cr (4*c*) atoms, CoMnCrGa exhibits all the signatures of HMF characteristic, *viz.*, adherence to Slater-Pauling (S-P) rule to isothermal saturation magnetization and absence of magnon scattering in temperature dependent resistivity data. Given its high T_C ($\sim$ 807 K), low magnetic moment and very high spin-polarization, the compound is a promising candidate for room temperature spintronics applications.

1 Introduction

Spintronics is a promising area of research for creating more efficient and powerful nanoelectronics. It aims to reduce power consumption and enhance memory and processing capabilities[1–4]. Materials with high spin-polarization are considered ideal for use in spintronics technology[5]. Half-metallic ferromagnetic (HMF) materials offer 100% spin polarization because of their unique band structure, where one sub-band conducts like a metal and the other acts like a semiconductor[6–9]. This unique band structure of HMF have made them attractive for a wide range of applications, including spintronics, data storage, magnetic sensors[5], spin valves[10], spin injectors[11], and magnetic tunnel junctions[12]. Out of different existing classes of HMF materials, Heusler alloys occupy a very special place as their electronic structure can be tuned over a wide range by appropriate elemental substitution at different crystal sites. Heusler alloys are generally denoted by the formula X_2YZ, where X and Y are transition elements and Z is from the *s-p* group element. These alloys have a $L2_1$ crystalline structure (Cu_2MnAl-type), in which the X, Y, and Z atoms occupy 8*c*, 4*b*, and 4*a* sites, respectively, in the $Fm\bar{3}m$ space group (no. 225)[13]. If one of the X atoms from X_2YZ is swapped with a different transition element (X'), it will result in a quaternary Heusler alloy with a Y-type crystal structure (LiMgPdSn type, space group: $F\bar{4}3m$, no. 216)[14–17]. As a result of this substitution, the crystal structure transforms to a lower symmetry space-group, where the 8*c* site in $Fm\bar{3}m$ space group splits into 4*c* and 4*d* sites in $F\bar{4}3m$ space group. Recently, quaternary Heusler alloys attracted a lot of attention of the research community due to their HMF[18–22], spin-gapless semiconductors[23–28], spin-semimetal[29], spin glass[30], re-entrant spin glass[31] and bipolar magnetic semiconducting properties[32]. However, the structural disorder, which is quite inherent for Heusler alloy, is known to have a significant impact on the magnetic as well as the electronic structure. The electronic structure of a material is altered by disorder, which changes the density of states, generates local magnetic moments, and narrows the band gap in the half-metallic ferromagnetic materials. These changes result in a reduced magnetic moment, lower magnetic ordering temperature[31,33], weakened magnetic anisotropy, and decreased electrical conductivity. It makes sense that in order to preserve the half-metallic ferromagnetic properties, either the compound must be synthesized without defects or one must find compounds where the properties are resilient to disorder. However, it is crucial to note that while theoretical predictions are promising[22,34–39], there are many more factors that are to

[a] *Condensed Matter Physics Division, Saha Institute of Nuclear Physics, A CI of Homi Bhabha National Institute, 1/AF Bidhannagar, Kolkata 700064, India*
[b] *Atomic & Molecular Physics Division, Bhabha Atomic Research Centre, Mumbai 400 094, India*
[c] *Ames National Laboratory, Iowa State University, Ames, Iowa 50011, USA*
[d] *Department of Condensed Matter Physics and Materials Science, Tata Institute of Fundamental Research, Homi Bhabha Road, Colaba, Mumbai 400005, India*
[e] *Univ Paris Est Creteil, CNRS, ICMPE, UMR 7182, 2 rue Henri Dunant, 94320 Thiais, France*
[f] *Beamline Development and Application Section Physics Group, Bhabha Atomic Research Centre, Mumbai 400085, India*
[g] *Australian Nuclear Science and Technology Organisation, Locked Bag 2001, Kirrawee DC, NSW 2232, Australia*
[h] *School of Chemistry, The University of Sydney, Sydney, NSW 2006, Australia*
∗ *chandan.mazumdar@saha.ac.in*

be considered before the experimental realizations of materials that can have potential for technological applications. Additionally, many of the predicted systems do not even form in single phase, and to the best of our knowledge, only few such compounds have been experimentally realized so far. Recently, FeMnVAl[19] and FeMnVGa[20] were found to show robust half-metallicity even in the presence of structural disorder. However, the Curie temperature for FeMnVAl is 213 K and for FeMnVGa is close to room temperature (293 K). For practical applications at room temperature, compounds having high transition temperature are highly desirable. In this study, we have reported a novel quaternary Heusler alloy CoMnCrGa, having the valence electron count (VEC) 25. Combining different experimental tools and theoretical DFT calculations, we have shown that the compound exhibits half-metallic ferromagnetic character despite having site disorder between Mn and Cr atomic sites. The compound orders ferromagnetically at a very hight temperature, 807 K, and hence is perfectly suitable for room temperature practical application in spintronics.

2 Methods

2.1 Experimental

The CoMnCrGa polycrystalline material was synthesized through an arc melting process utilizing high purity (>99.9%) constituent elements. An extra 2% of Mn was added to make up for its evaporation during the process. To enhance homogeneity, the sample was melted 5-6 times in an argon environment and turned over after each melting. Both neutron and X-ray diffraction techniques were used to characterize the sample's crystal structure at room temperature. The powder neutron diffraction data with $\lambda = 2.43$ Å was collected at 300 K at the ECHIDNA beamline in ANSTO, Australia[40]. Room temperature powder X-ray diffraction pattern was obtained using a X-ray diffractometer (TTRAX-III, Rigaku Corp., Japan) with Cu-Kα radiation. The single-phase nature and crystal structure of the sample were determined through Rietveld refinement[41] of both the neutron and X-ray diffraction data using the FULLPROF software. Extended X-ray absorption fine structure (EXAFS) was obtained at the Energy Scanning EXAFS beamline (BL-9) located at the Raja Ramanna Centre for Advanced Technology (RRCAT) in Indore, India. Standard EXAFS measurements protocols have been used as detailed elsewhere[20,31]. High-temperature VSM (Model EV9, MicroSense, LLC Corp., USA) was used to measure the magnetization (M) *vs.* temperature (T) in the range of 300–900 K. M *vs.* field (H) measurement was carried out using superconducting quantum interference vibrating sample magnometer (Quantum design Inc.,USA) in the magnetic fields up to $\pm$70 kOe at 5 K. Four-probe resistivity measurement in the absence of magnetic field was carried out in a Physical Property Measurement System (Quantum Design Inc., USA).

2.2 Computational

The enthalpy of formation, electronic structure and spin polarization at 0 K had been determined through DFT calculations using the projector augmented wave (PAW) method[42] implemented in the Vienna ab initio simulation package (VASP)[43,44]. The exchange-correlation was described by the generalized gradient approximation modified by Perdew, Burke and Ernzerhof (GGA-PBE)[45]. Calculations parameters were discussed in detail elsewhere in literature[19,20,31].

Table 1 Different types of ordered structure of CoMnCrGa

	4*a*	4*b*	4*c*	4*d*
Type 1	Ga	Cr	Mn	Co
Type 2	Ga	Mn	Cr	Co
Type 3	Ga	Co	Mn	Cr

3 Results and discussion

3.1 Electronic band structure calculations

There are four different crystallographic sites in a quaternary Heusler $XX'YZ$: 4*a* (0,0,0), 4*b* (0.5,0.5,0.5), 4*c* (0.25,0.25,0.25) and 4*d* (0.75,0.75,0.75). In most cases, the *sp* element *Z* occupies the 4*a* position and the transition metals are located on the other three sites. In total, 6 configurations are possible but the permutation of the atoms in the 4*c* and 4*d* positions leads in energetically invariant configurations. Hence, only three independent configurations have been calculated. These configurations are defined as Type-1, 2 and 3 and described in Table 1. The DFT calculations allow to determine the most stable structure by comparing their enthalpies of formation.

According to our calculations on the ordered structure, Type-2 is the most stable configuration, with Ga in the 4*a* position and Mn in the 4*b* position, Cr at 4*c* and Co at the 4*d* position. Fig. 1 shows for the calculated spin-polarised band structure and the density of states (DOS) for the Type-2 configuration. As shown in the DOS, the spin-down band exhibits a band gap at the Fermi level (E_F) where the spin-up band is typical of a metal. This unique band structure corresponds to that of a Half-Metallic Ferromagnetic material. This result is confirmed by the very high polarisation of the compound, $P = \frac{DOS^{\uparrow}(E_F) - DOS^{\downarrow}(E_F)}{DOS^{\uparrow}(E_F) + DOS^{\downarrow}(E_F)} = 96.1\%$. The total magnetic moment is estimated to be 1.06 μ_B which is in accordance with the Slater-Pauling rule[46–48]. Fig. 2 represents the partial density of states for the studied compound. The element specific magnetic moments are estimated to be Cr: -2.47 μ_B Co: 0.70 μ_B Mn: 2.88 μ_B and Ga: -0.05 μ_B.

3.2 Neutron diffraction

All the constituents elements (Co, Mn, Cr and Ga) of the studied compounds belongs from the same row of periodic table and have close-by X-ray scattering factors. As a result, X-ray diffraction (XRD) data is not likely to be reliable for determining the actual crystal structure (discussed in detail in Sec. 3.3). Extended X-ray fine structure (EXAFS) measurement, however can satisfactorily provide the information about the crystalline disorder, particularly when the disorder is of B2 type[49,50]. On the other hand, EXAFS fails when the disorder is of DO_3 type[51]. Neutron diffraction have already proved their merits for such difficult cases[20,31,33,52,53]. Fig. 3 represents the powder neutron diffraction pattern taken at 300 K. For Heusler alloys, presence of (111) and (200) Bragg peaks in the diffraction pattern are gener-

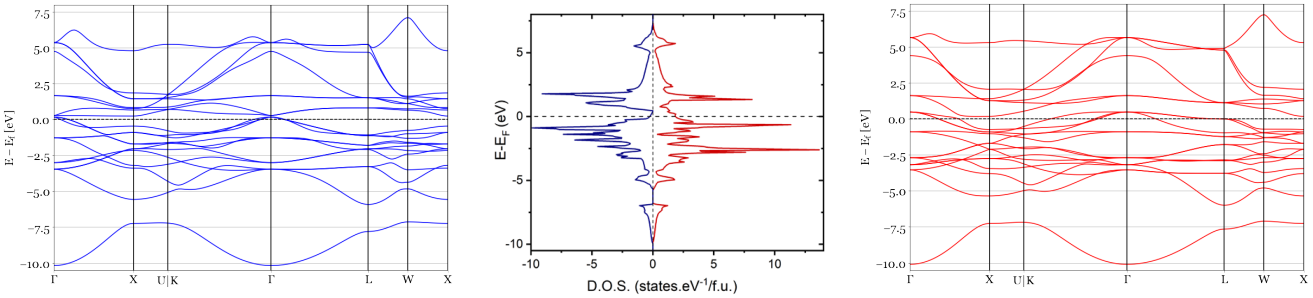

(a) Minority Spin (b) Density of states (c) Majority Spin

Fig. 1 Spin-polarized band structure and density of states of CoMnCrGa in ordered Type 2 structure: (a) minority spin band (b) density of states, (c) majority spin band.

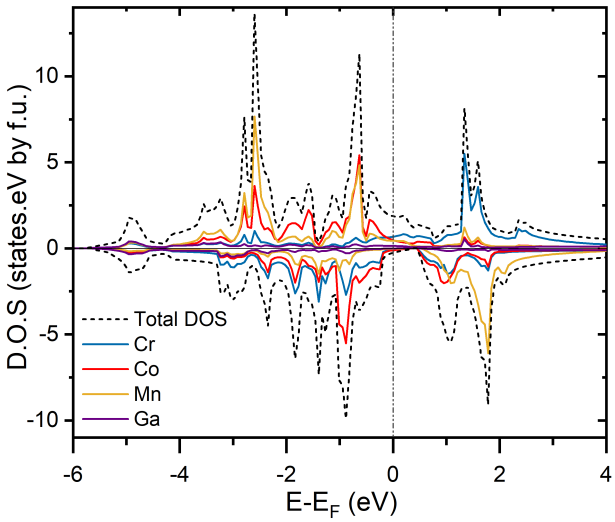

Fig. 2 Electronic DOS (total and partial) of CoMnCrGa.

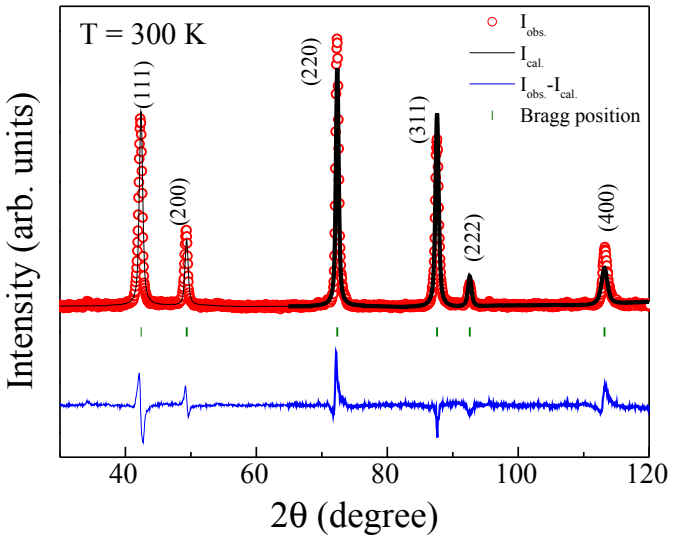

Fig. 3 Rietveld refinement of the neutron diffraction pattern (taken at 300 K) of CoMnCrGa, considering the crystal structure only.

ally considered to be indicative of well-ordered crystal structure. As it can be clearly seen in the diffraction pattern of CoMnCrGa (Fig. 3), both the above mentioned peaks are present, indicating towards an ordered structure. However, despite the presence of (111) and (200) Bragg peaks, the intensities of all the experimental data cannot be described by a simple ordered Type-2 structure, as proposed by DFT calculation (Sec. 3.1) in which Ga is at 4*a*, Mn at 4*b*, Cr at 4*c* and Co at 4*d* (space group: $F\bar{4}3m$, no. 216). We have tried different combinations of anti-site and swap disorder to fit the diffraction data. A swap disorder of 55:45 between Mn (4*b*) and Cr (4*c*) sites in the space group: $F\bar{4}3m$ fits the experimental data very well. The disordered structure is presented in Fig. 4. The shape of the peak is not very well fitted, this can result from some anisotropic peak broadening related to the Mn/Cr disorder. It may however be noted that, as we will see later (Sec. 3.6), the compound orders magnetically at 807 K, and hence the ND spectra at 300 K would also consists of magnetic contribution. However, for a VEC 25 compound, as is the case of CoMnCrGa, the S-P rule suggests the maximum magnetic moment to be 1 μ_B/f.u. (Sec. 3.6). The contribution to magnetic Bragg peaks are not known to yield more than 2-3% of nuclear Bragg peaks[20,31,33]. Therefore, our analysis of ND spectra at 300 K considering only the lattice Bragg contributions would not be far off from that expected for a paramagnetic state.

3.3 X-ray diffraction

We have also measured the XRD pattern at room temperature and analysed the data, to check the structural model derived from the neutron diffraction result. Moreover, the shorter wavelength used in XRD measurement, in comparison to neutron diffraction measurement, also helps us to determine the lattice parameter more precisely. Very interestingly, the (111) and (200) Bragg peaks, which are generally considered to be indicative of crystal order and prominently present in the ND data (Fig. 3), are almost completely absent in XRD data. A simulation of XRD pattern considering the perfectly ordered Type-2 structure (Fig. 5) also does not show these Bragg peaks any prominently due to the close by X-ray scattering factors of the constituents elements. The scattering factor for (111) and (200) planes can be written as[30]

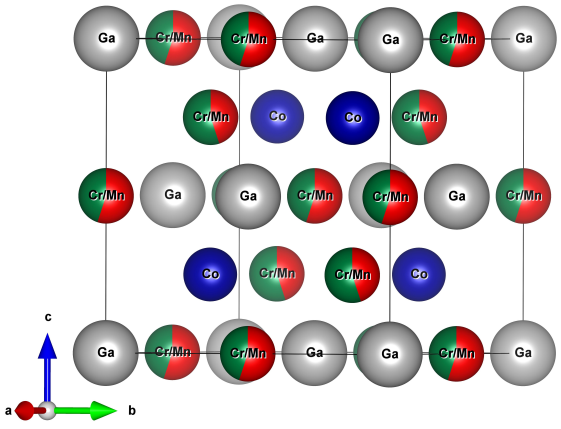

Fig. 4 Atomic arrangements in disordered structure. Grey, blue, olive and blue color represents Ga, Co, Cr and Mn atoms respectively.

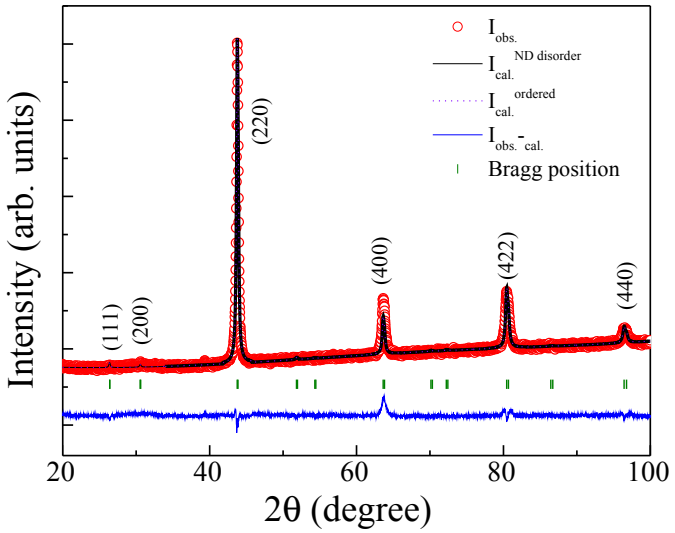

Fig. 5 Rietveld refinement of the powder XRD pattern of CoMnCrGa assuming disordered structure & ordered structure measured at room temperature. The two fits got overlapped and remain essentially indistinguishable. Bragg peaks are mentioned in vertical first bracket.

$$F_{111} = 4(f_Z - f_Y) - i(f_X - f_{X'}))$$

$$F_{200} = 4[(f_Z + f_Y) - (f_X + f_{X'})]$$

Since all the elements of CoMnCrGa belongs to the same row of the periodic table, f_Z - $f_Y \approx 0$, f_X - $f_{X'} \approx 0$, f_Z + $f_Y \approx f_X$ + $f_{X'}$. Because of the very faint or non-discernible nature of (111) and (200) peaks in the simulated diffraction pattern of the ordered structure, the experimental XRD pattern can be explained well with ordered structure. However, the XRD analysis also shows almost equally good fit, if not slightly better, if we use the structural model obtained from neutron diffraction analysis. Since the disordered structure can simultaneously explain both the ND as well as XRD data, one is inclined to rely on the structural model obtained from analysis of ND data. Fig. 5 represents the Rietveld refinement of the powder XRD data assuming the disordered structure taken at room temperature. The lattice parameter is found to be a = 5.841(3) Å.

3.4 Transmission electron microscopes (TEM) Analysis and Chemical Composition

Fig. 6(a) represents Transmission Electron Microscopy (TEM) image, replete with discernible thickness fringes traversing the micrograph. This portrayal exposes intricate nanoscale structural features. The selected area electron diffraction (SAED) pattern from a region marked by a dotted circle is shown in Fig. 6(b), which indicates the single crystalline nature of the material. SAED was indexed using the lattice parameters of cubic crystal structure (lattice parameters, a = 5.841 Å). To investigate the chemical composition of the compound, we have performed energy dispersive X-ray spectroscopy (EDX) in high-angle annular dark field (HAADF) scanning transmission electron microscopy (STEM-HAADF) mode. Fig. 6(c) shows the STEM-HAADF image, and Fig. 6(d) showing EDX spectrums take at point 1 indicated in Fig. 6(c), clearly showing the presence of Co, Mn, Cr and Ga. Fig. 6(e) represents the EDX line-profile analysis performed along Line 2 in image Fig. 6(c). For a detailed distribution of atomic content, elemental mapping of Co, Mn, Cr and Ga were performed using drift corrected EDX spectrum imaging using STEM-HAADF mode. The STEM-HAADF image in Fig. 6(c) and the corresponding chemical maps from orange-boxed region (marked 3 in Fig. 6(c)) for Co, Mn, Cr and Ga acquired using Co-L, Mn-K Cr-K and Ga-K energy and overlay of three images are presented in Fig. 6(f), respectively. Composite maps of Co, Mn, Cr and Ga were presented in Fig. 6(f) confirm the single phase nature of the material with stoichiometry $Co_{0.98}MnCr_{0.9}Ga_{0.92}$.

3.5 EXAFS

In our studied compound, the structural disorder is neither B2-type nor DO_3-type. To get any insight of structural disorder between Mn (4*b*) and Cr (4*c*) atoms, we have probed the system using EXAFS, which in contrast to XRD, concentrates on the atomic surroundings of the chosen atoms. In order to study the local environment of the Co, Mn, and Cr edges, we performed EXAFS measurements on CoMnCrGa.

The normalized EXAFS ((μ(E) versus E) spectra, measured at the Co, Mn, and Cr edges, are shown in Fig. 7. The conventional technique was followed in processing the analysis of the EXAFS data[54]. Briefly, the absorption spectra (μ(E) vs E) have been transformed to the absorption function χ(E) given as follows to get quantitative information on the local structure.

$$\chi(E) = \frac{\mu(E) - \mu_0(E)}{\Delta\mu_0(E_0)} \quad (1)$$

where $\mu_0(E_0)$ is the background made up entirely of bare atoms, $\Delta\mu_0(E_0)$ is the absorption edge step in $\mu(E)$ value, and E_0 is the absorption edge energy. The following relation converts the energy dependent absorption coefficient $\chi(E)$ to the wave number dependent absorption coefficient:

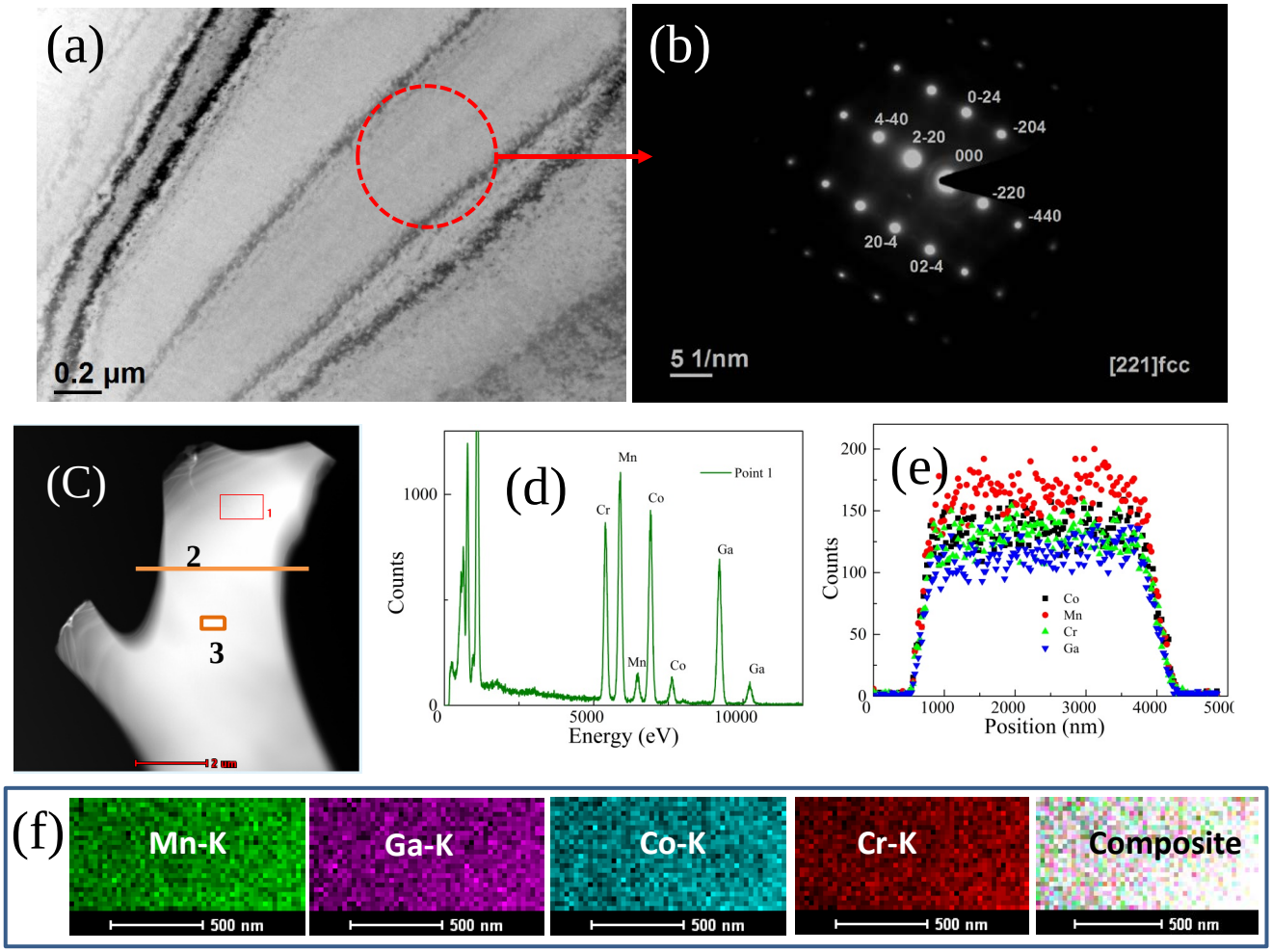

Fig. 6 (a) TEM image (thickness fringes running over the image) (b) Selected area electron diffraction (c) Scanning TEM-High angle annular dark-field image (d) Energy dispersive X-ray (EDX) spectrum from point 1 (e) EDX line-profile from line 2 in (c) (f) Elemental mapping from area 3 in (c).

$$K = \sqrt{\frac{2m(E - E_0)}{\hbar^2}} \tag{2}$$

where m is the mass of an electron. To increase the oscillation at high k, $\chi(k)$ is weighted by k^2, and the resulting $\chi(k)k^2$ functions are then Fourier converted in R space to produce the $\chi(R)$ versus R plots in terms of the actual distances from the absorbing atom's center. The aforementioned data reduction, which includes background reduction and Fourier transformation, was carried out using the ATHENA subroutine, which is a component of the Demeter software package[55]. The CoMnCrGa sample's Fourier converted EXAFS spectra at the Co, Mn, and Cr edges are presented in Fig. 8 as χ(R) versus R plots.

The goodness of fit has been determined by the value of the R_{factor} defined by:

$$R_{factor} = \frac{[Im(\chi_{dat}(r_i) - \chi_{th}(r_i)]^2 + [Re((\chi_{dat}(r_i) - \chi_{th}(r_i)]^2]^2}{[Im(\chi_{dat}(r_i)]^2 + [Re(\chi_{dat}(r_i)]^2} \tag{3}$$

where, χ_{dat} and χ_{th} refer to the experimental and theoretical values respectively and *Im* and *Re* refer to the imaginary and real parts of the respective quantities. The Demeter software package's ATOMS and ARTEMIS subroutines have been used to generate theoretical routes from crystallographic structures and fit experimental data to theoretical simulations, respectively. The best fit of theoretical spectra and experimental data are shown together in Fig. 8, and the best fit parameters are included in Table 2. EXAFS data can be fitted very well assuming Type-2 ordered structure. As mentioned earlier (Sec. 3.2), since the structural disorder we derive from the analysis of ND data is not of B2 type, EXAFS analysis can not detect the atomic disorder present in the system due to the close by scattering factors between Mn and Cr atoms.

3.6 Magnetic properties

DFT calculations suggest that the ground state of CoMnCrGa is half-metallic ferromagnetic. To check whether the compound really orders ferromagnetically or not and also to determine the magnetic ordering temperature, if any, we have measured temperature dependence of the magnetization (M) in presence of 100 Oe applied magnetic field. Indeed, the compound orders ferromagnetically, and the Curie temperature is found quite high, ~807 K, making it suitable for any ferromagnetic application at

Table 2 Bond length (R), coordination number (N), and Debye-Waller or disorder factor (σ^2) obtained by EXAFS fitting for CoMnCrGa at Co, Mn and Cr edge.

Co edge				Mn edge				Cr edge			
Path	R (Å)	N	σ^2	Path	R (Å)	N	σ^2	Path	R (Å)	N	σ^2
Co-Cr	2.42±0.01	4	0.0277±0.0030	Mn-Ga	2.42±0.01	4	0.0143±0.0022	Cr-Mn	2.42±0.01	4	0.0143±0.0022
Co-Ga	2.42±0.01	4	0.0060±0.0009	Mn-Cr	2.42±0.01	4	0.0277±0.0030	Cr-Co	2.42±0.01	4	0.0277±0.0030
Co-Mn	2.82±0.01	6	0.0062±0.0010	Mn-Co	2.82±0.01	6	0.0062±0.0010	Cr-Ga	2.81±0.01	6	0.0062±0.0010
Co-Co	4.10±0.01	12	0.0168±0.0024	Mn-Mn	4.14±0.01	12	0.0182±0.0043	Cr-Cr	4.12±0.04	12	0.0182±0.0043
Co-Cr	4.88±0.04	12	0.0109±0.0068	Mn-Ga	4.92±0.01	12	0.0160±0.0033	Cr-Mn	4.89±0.02	12	0.00160±0.0033
Co-Ga	4.88±0.04	12	0.0091±0.0050	Mn-Cr	4.92±0.01	12	0.0083±0.0012	Cr-Co	4.89±0.02	12	0.0083±0.0012

room temperature. The other theoretical prediction, i.e. the presence of HMF state can be also checked by measuring the saturation magnetization at low temperature. All the known Heusler based HMF materials are known to follow the Slater-Palling (S-P) rule, which relates the total valence electron count (VEC) with the saturation magnetization. The S-P rule states that the total magnetic moment for Heusler alloy can be expressed as m = (VEC-24) μ_B. Since CoMnCrGa has VEC 25, the S-P rule predicts the saturation moment to be (25-24 =) 1 μ_B/f.u. The experimentally observed saturation magnetization measured at 5 K (Fig. 10) indeed matches very closely to the theoretically predicted S-P rule with 1 μ_B/f.u. This value is also in agreement with the DFT calculation (Sec. 3.1), suggesting CoMnCrGa to have a half-metallic ferromagnetic ground state.

3.7 Resistivity

HMF materials are also known to show their signatory imprint on the electrical transport properties[19,20,56]. We have measured resistivity, ρ(T), in the temperature regime 5-300 K (Fig. 11). The residual resistivity ratio (RRR=ρ_{300K}/ρ_{5K}) found to be quite low, ∼1.05, similar to that reported earlier in many other HMF Heusler alloys[19,20,57,58]. However, in the present case, the ρ(T) behaviour shows an additional broad minima near 60 K, followed by a slow upturn at further lower temperatures. Such behaviour is generally attributed to the disorder-induced coherent scattering of conduction electrons, known as weak localization[59], and also reported in several Heusler alloys[60–63].

To analyze the ρ(T) data over the whole temperature range, we have followed the Matthiessen's rule covering various contributing factors in a ferromagnetic material[15]. The said rule considers all the scattering processes to be independent of one another and additive. Accordingly, the total resistivity can be expressed as

$$\rho(T) = \rho_0 + \rho_P(T) + \rho_M(T) \quad (4)$$

where ρ_0 is the residual resistivity resulting from lattice flaws, irregularities, etc., and ρ_P(T) and ρ_M(T) are temperature-dependent factors, representing phonon scattering and magnon scattering, respectively. The phonon scattering term is generally written as

$$\rho_P = A\left(\frac{T}{\Theta_D}\right)^5 \int_0^{\frac{\Theta_D}{T}} \frac{x^5}{(e^x-1)(1-e^{-x})} dx \quad (5)$$

where A is the phonon scattering constant and Θ_D is the Debye temperature[64]. The standard magnon contribution due to spin-flip scattering (∼T^2) are generally not found for HMF materials, as one of the sub-spin band do not have any influence to charge conduction[19,20]. Considering the aforementioned information and taking the magnon contribution to be zero, we have first tried to fit the resistivity data using eqn. 4. The theoretically generated data fit the experimental data very well in the region 300-100 K, however it fails to trace the experimental data in the low temperature region (5-100 K). The non-adherence of ρ(T) to eqn. 4 is due to the development of another contribution to resistivity at lower temperature that causes a slow upturn in ρ(T), below 60 K as described earlier in the beginning of this section. To fit the low temperature resistivity data we have used another following equation

$$\rho(T) = \rho_0 - BT^{1/2} + CT^5 + DT^2 \quad (6)$$

where -$BT^{1/2}$ arises due to the disorder increased coherent scattering of conduction electrons[59], CT^5 is the low temperature phonon contribution (can be easily derived from eqn. 5 for low temperature approximation) and DT^2 is the electron-electron scattering. The eqn. 6 fits the experimental data well in the low temperature regime (inset of Fig. 11). The absence of magnon contribution in the temperature dependent resistivity data indirectly suggests towards presence of half-metallic ferromagnetic ground state.

3.8 Anomalous Hall measurement

Hall measurements were conducted over a temperature range spanning from 5–300 K to investigate the charge transport characteristics of CoMnCrGa. Generally, the total Hall resistivity (denoted as ρ_H) can be divided into two components: the ordinary Hall effect and the anomalous Hall effect (AHE). Mathematically, it can be expressed as[65]:

$$\rho_H = R_0 H + R_S M_S \quad (7)$$

Here, R_0 represents the ordinary Hall coefficient, R_S is the anomalous Hall coefficient, and M_S signifies the saturation magnetization. The product $R_S M_S$ quantifies the magnitude of the anomalous Hall resistivity (ρ_{AH}). Field-dependent data for ρ_H were recorded at various temperatures, up to a maximum magnetic field of 70 kOe, as depicted in Fig 12(a). The ρ_{AH} exhibits a sharp increase up to a 3 kOe magnetic field due to the AHE. At higher magnetic field strengths (> 3 kOe), ρ_{AH} exhibits a linear

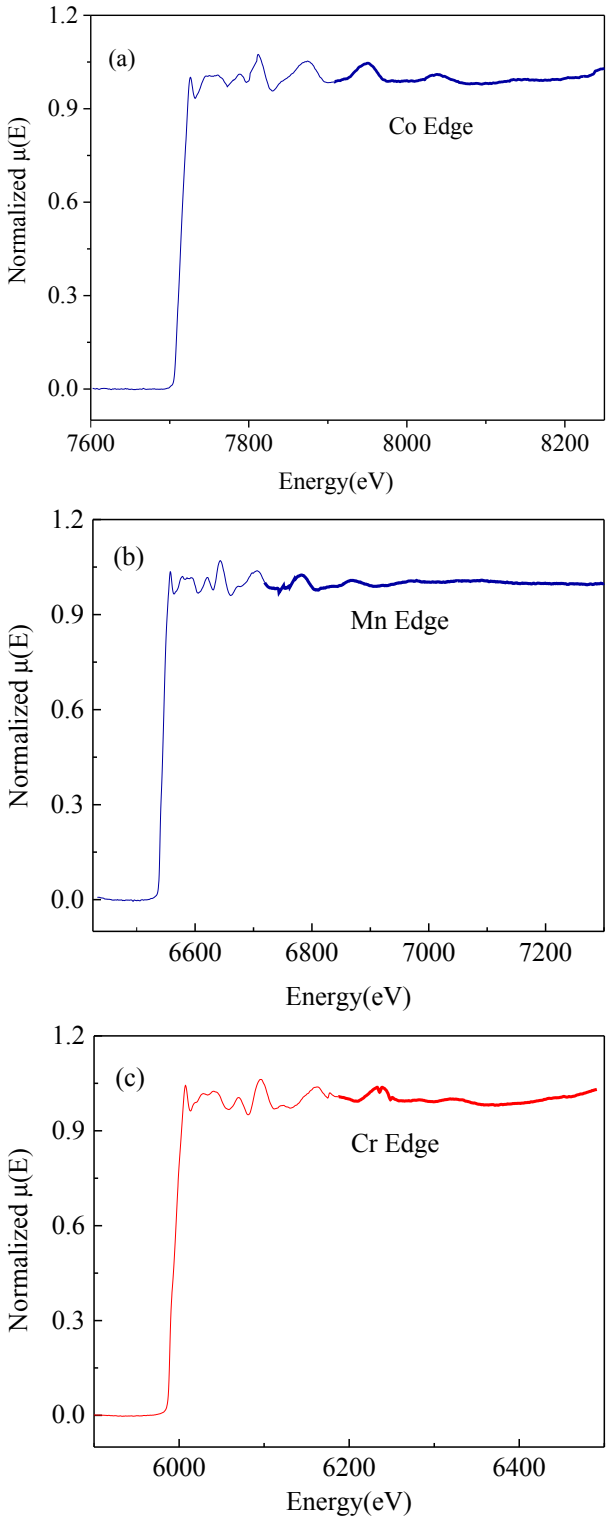

Fig. 7 Normalized EXAFS spectra of CoMnCrGa taken at (a) Co edge (b) Mn edge and (c) Cr edge.

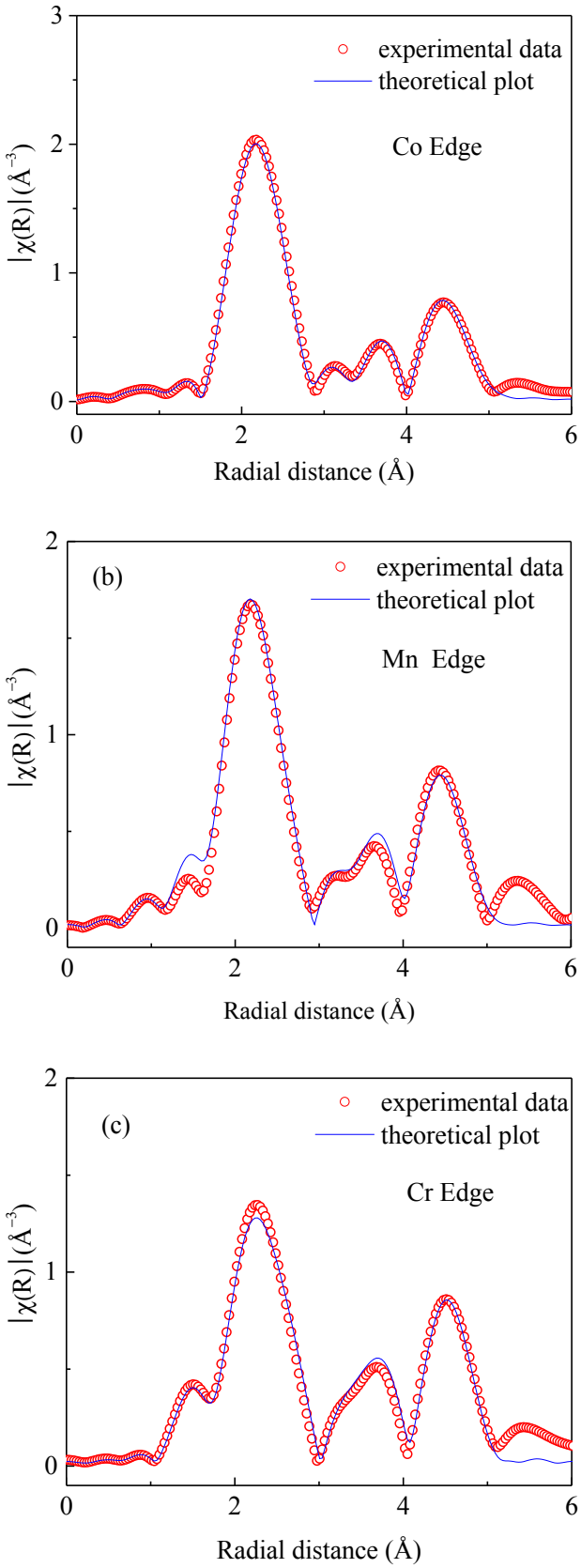

Fig. 8 Fourier transformed EXAFS spectra of CoMnCrGa taken at Co, Mn and Cr edges.

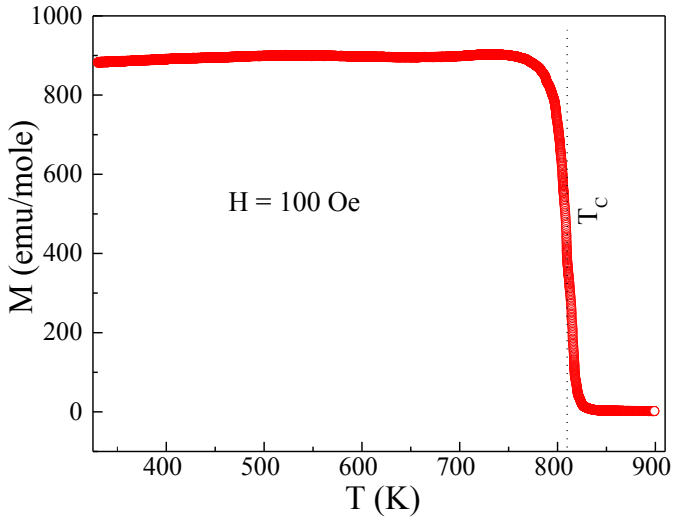

Fig. 9 Temperature dependence of magnetic susceptibility of CoMnCrGa measured in a 100 Oe applied magnetic field. Curie temperature, T_C, is determined from the minima in dM/dT *vs.* T plot.

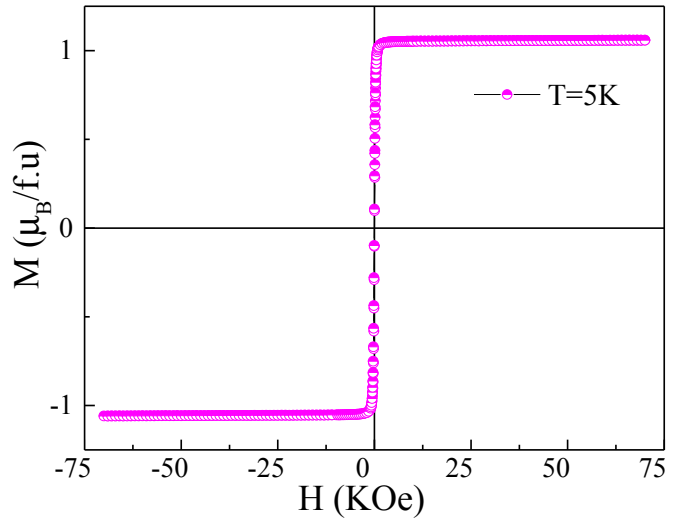

Fig. 10 Isothermal magnetization of CoMnCrGa measured at 5 K.

increase with a positive slope, which is attributed to the ordinary Hall effect. To distinguish between the ordinary and anomalous Hall contributions, we applied a fitting procedure using Eqn. 7 in the high-field region. This fitting yielded the values of R_0 and $R_S M_S$, corresponding to the slope and intercept on the y-axis of the fitted line, respectively.

The consistently positive value of R_0 across the entire temperature range (5–300 K) suggests that holes are the dominant charge carriers in the transport process. The carrier concentration (n), determined by the expression $n = \frac{1}{eR_0}$, was found to be 10^{22}, and its temperature dependence is illustrated in the inset of Fig 12(a). The Hall conductivity (σ_H) was determined using the equation[66]:

$$\sigma_H = \frac{\rho_H}{(\rho_H{}^2 + \rho_{xx}{}^2)} \tag{8}$$

The field-dependent Hall conductivity taken at various temperatures are presented in Fig 12(b), where the anomalous Hall con-

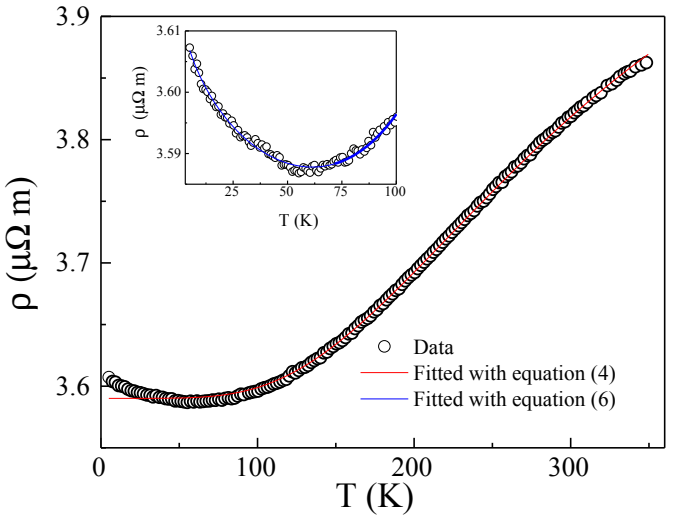

Fig. 11 Temperature dependence of the electrical resistivity measured in the absence of magnetic field in the temperature range 5−300 K.

ductivity (AHC) were determined by extrapolating the high-field Hall conductivity data to zero field. The obtained value of AHC is 22 S/cm at 5 K. To discern the individual contributions of extrinsic and intrinsic mechanisms to the overall AHC, we analyzed the $\frac{\rho_{AH}}{\rho_{xx}}$ versus ρ_{xx} data (depicted as blue triangles in Fig 12(d)) and fitted it with the following relation[67]:

$$\frac{\rho_{AH}}{\rho_{xx}} = a + b\rho_{xx} \tag{9}$$

In this equation, the parameters a and b contain information about extrinsic skew scattering and the combined effects of extrinsic side jump and intrinsic contributions, respectively. The fitting yielded values of $a = -0.001$ and $b = 28$ S/cm. The negative value of coefficient a implies that the extrinsic skew scattering contribution opposes both the side jump and intrinsic contributions due to momentum space Berry curvature. The parameter b encompasses the contributions to AHC from both the side jump and momentum space Berry curvature. By using these coefficients a and b, we calculated the skew scattering term ($a\rho_{xx}$) and the intrinsic plus side jump term ($b\rho_{xx}{}^2$) and plotted them on the same scale, as shown in Fig 12(c). It is evident that the side jump, in conjunction with the intrinsic contribution, dominates over the skew scattering contribution in the overall AHE within the temperature range of 5–300 K. The AHC arising from the side jump mechanism can be approximated using the expression $\frac{e^2}{\hbar a}.\frac{E_{so}}{E_F}$ where E_{so} represents the spin-orbit interaction energy, and E_F is the Fermi energy[68,69]. It is worth noting that $\frac{E_{so}}{E_F}$ is typically less than 0.01 for ferromagnetic metals, indicating that the intrinsic Berry-phase-driven contribution predominantly governs the AHC, which is also evident from Fig 12(c).

4 Conclusion

To summarize, the structural, electronic, magnetic, and transport properties of a new quaternary Heusler alloy CoMnCrGa were investigated using both experimental and theoretical methods. First principle calculations reveals half-metallic ferromagnetic ground

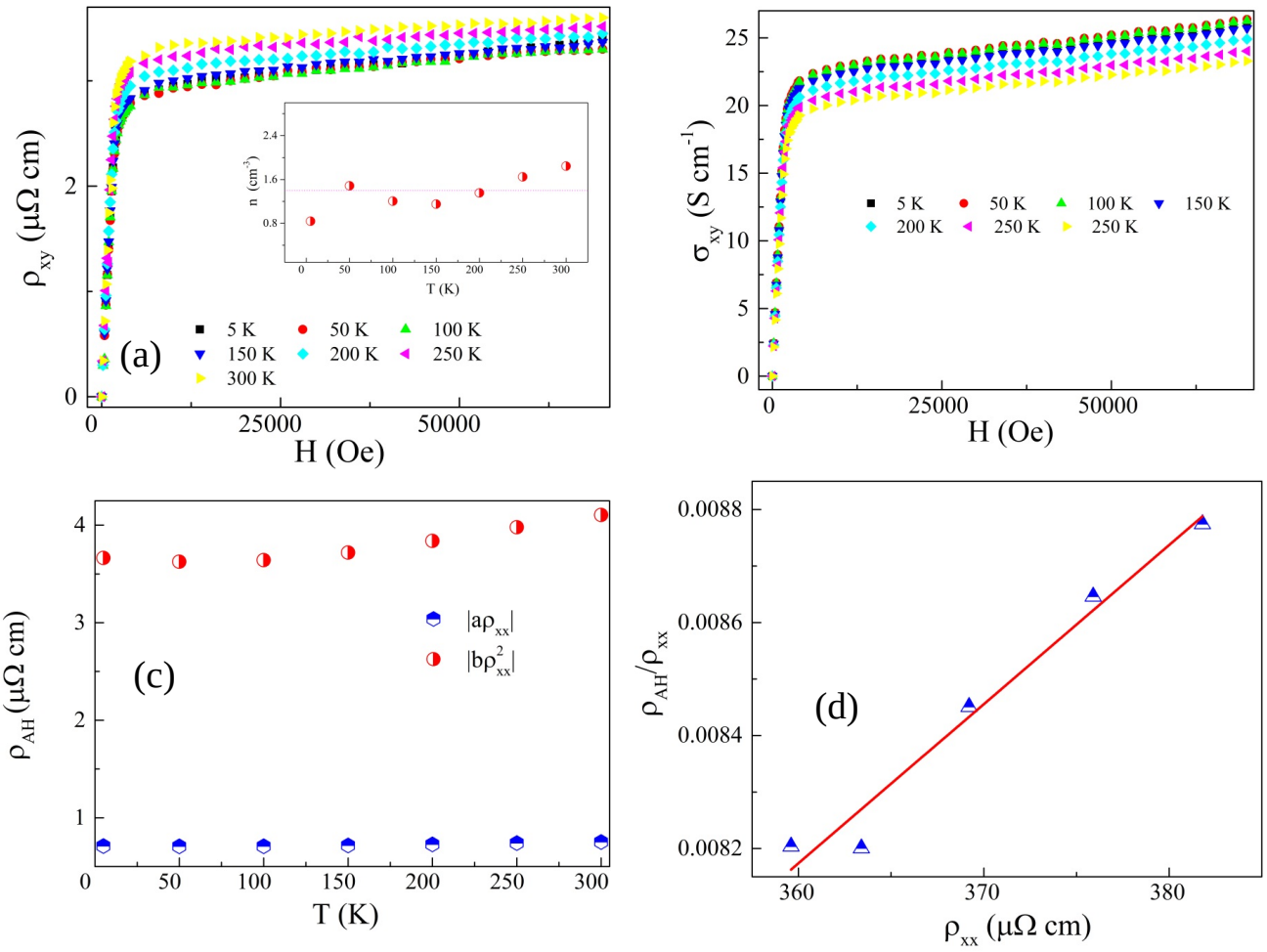

Fig. 12 (a) Field-dependent Hall resistivity curves at different temperatures. Inset shows temperature variations of carrier concentration (b) Field-dependent Hall conductivity curves at different temperatures. (c) Different contributions in ρ_{AH} with temperature are plotted on the same scale. (d) Fitting of the ratio of anomalous Hall resistivity and longitudinal resistivity.

state in this material. Neutron diffraction experiment reveals that the compound crystalizes in disordered structure in which Mn (4*b*) and Cr (4*c*) atoms mixes with each other in 55:45 ratio. Despite the structural disorder, the material is found to order ferromagnetically at a very high temperature (~807 K) and the total saturation magnetization follows the S-P rule, commensurate with the HMF characteristics predicted from DFT calculation. The absence of magnon contribution in the resistivity data further supports the presence of HMF state. High value of the T_C along with high spin polarized ferromagnetic state in this structurally disordered compound makes it perfectly suitable for for practical application in the field of room temperature spintronics. The low magnetic moment of CoMnCrGa is also advantageous for spintronics applications. It results in a negligible stray magnetic field, which is desirable in devices where magnetic interference needs to be minimized. Additionally, a lower switching current is required to flip the spin direction of this alloy, enhancing its energy efficiency.

Author Contributions

S.Gupta and conceived, planned, and carried out the experiments and analyzed the data. S.Chakraborty, S. Pakhira and S. Dan helped during experiments and data analysis. V. Bhasin, S.N. Jha and D. Bhattacharyya performed and analyzed the EXAFS data. C. Barreteau and J.C. Crivello performed the DFT calculations. M. Avdeev and V.P. Boncour helped in neutron diffraction experiment and analysis. C. Mazumdar supervised the project. All authors discussed the results and contributed to the final manuscript.

Conflicts of interest

The authors declare that they have no known competing financial interests or personal relationships that could have appeared to influence the work reported in this paper.

Acknowledgements

S.G and S.C would like to sincerely acknowledge SINP, India and UGC, India, respectively, for their fellowship. The authors would like to sincerely thank Prof. Biswarup Satpati, SINP, for

the TEM & EDX measurements. DFT calculations were performed using HPC resources from GENCI-CINES (Grant 2021-A0100906175). Work at the Ames Laboratory (in part) was supported by the Department of Energy- Basic Energy Sciences, Materials Sciences and Engineering Division, under Contract No. DE-AC02-07CH11358.

Notes and references

1 I. Žutić, J. Fabian and S. D. Sarma, *Reviews of modern physics*, 2004, **76**, 323.
2 F. Pulizzi, *Nature materials*, 2012, **11**, 367–367.
3 D. D. Awschalom and M. E. Flatté, *Nature physics*, 2007, **3**, 153–159.
4 T. V. Vu, D. K. Nguyen, J. Guerrero-Sanchez, J. Rivas-Silva, G. H. Cocoletzi and D. Hoat, *RSC advances*, 2022, **12**, 26418–26427.
5 C. Felser, G. H. Fecher and B. Balke, *Angewandte Chemie International Edition*, 2007, **46**, 668–699.
6 R. De Groot, F. Mueller, P. v. van Engen and K. Buschow, *Physical review letters*, 1983, **50**, 2024.
7 M. Katsnelson, V. Y. Irkhin, L. Chioncel, A. Lichtenstein and R. A. de Groot, *Reviews of Modern Physics*, 2008, **80**, 315.
8 X. Wang, T. Lin, H. Rozale, X. Dai and G. Liu, *Journal of Magnetism and Magnetic Materials*, 2016, **402**, 190–195.
9 L. Siakeng, G. M. Mikhailov and D. Rai, *Journal of Materials Chemistry C*, 2018, **6**, 10341–10349.
10 Ikhtiar, S. Kasai, A. Itoh, Y. Takahashi, T. Ohkubo, S. Mitani and K. Hono, *Journal of Applied Physics*, 2014, **115**, 173912.
11 T. Saito, N. Tezuka, M. Matsuura and S. Sugimoto, *Applied Physics Express*, 2013, **6**, 103006.
12 T. Kubota, S. Tsunegi, M. Oogane, S. Mizukami, T. Miyazaki, H. Naganuma and Y. Ando, *Applied Physics Letters*, 2009, **94**, 122504.
13 C. Felser and A. Hirohata, *Heusler alloys*, Springer, 2015.
14 X. Dai, G. Liu, G. H. Fecher, C. Felser, Y. Li and H. Liu, *Journal of Applied Physics*, 2009, **105**, 07E901.
15 L. Bainsla and K. Suresh, *Applied Physics Reviews*, 2016, **3**, 031101.
16 P.-R. Cha *et al.*, *Journal of Materials Chemistry C*, 2019, **7**, 7664–7671.
17 J. Zhang, X. Li and J. Yang, *Journal of Materials Chemistry C*, 2015, **3**, 2563–2567.
18 D. Rani, K. Suresh, A. Yadav, S. Jha, D. Bhattacharyya, M. R. Varma, A. Alam *et al.*, *Physical Review B*, 2017, **96**, 184404.
19 S. Gupta, S. Chakraborty, S. Pakhira, C. Barreteau, J.-C. Crivello, B. Bandyopadhyay, J. M. Greneche, E. Alleno and C. Mazumdar, *Physical Review B*, 2022, **106**, 115148.
20 S. Gupta, S. Chakraborty, V. Bhasin, S. Pakhira, S. Dan, C. Barreteau, J.-C. Crivello, S. N. Jha, M. Avdeev, J.-M. Greneche, D. Bhattacharyya, E. Alleno and C. Mazumdar, *Phys. Rev. B*, 2023, **108**, 045137.
21 N. Kaur, R. Sharma, V. Srivastava and S. Chowdhury, *The Journal of Chemical Thermodynamics*, 2023, 107089.
22 R. Prakash and G. Kalpana, *RSC advances*, 2023, **13**, 10847–10860.
23 L. Bainsla, A. Mallick, M. M. Raja, A. Nigam, B. C. S. Varaprasad, Y. Takahashi, A. Alam, K. Suresh and K. Hono, *Physical Review B*, 2015, **91**, 104408.
24 L. Bainsla, A. Mallick, M. M. Raja, A. Coelho, A. Nigam, D. Johnson, A. Alam and K. Suresh, *Physical Review B*, 2015, **92**, 045201.
25 S. Gupta, J. Sau, M. Kumar and C. Mazumdar, *arXiv preprint arXiv:2303.08589*, 2023.
26 G. Li, Q. Sun, L. Xu, G. Liu and Z. Cao, *Journal of Materials Chemistry C*, 2023.
27 V. Mishra, A. Kumar, L. Pandey, N. K. Gupta, S. Hait, V. Barwal, N. Sharma, N. Kumar, S. Chandra and S. Chaudhary, *Nanoscale*, 2023, **15**, 337–349.
28 X. Wang, Z. Cheng, J. Wang, X.-L. Wang and G. Liu, *Journal of Materials Chemistry C*, 2016, **4**, 7176–7192.
29 Y. Venkateswara, S. S. Samatham, P. Babu, K. Suresh and A. Alam, *Physical Review B*, 2019, **100**, 180404.
30 S. Gupta, S. Chakraborty, S. Pakhira, A. Biswas, Y. Mudryk, A. Kumar, B. Mukherjee, G. S. Okram, A. Das, V. K. Pecharsky and C. Mazumdar, *Phys. Rev. B*, 2023, **107**, 184408.
31 S. Gupta, S. Chakraborty, V. Bhasin, S. Pakhira, A. Biswas, Y. Mudryk, A. Kumar, C. Barreteau, J.-C. Crivello, A. Das, S. N. Jha, D. Bhattacharyya, V. K. Pecharsky, E. Alleno and C. Mazumdar, *Phys. Rev. B*, 2023, **108**, 054405.
32 J. Nag, D. Rani, J. Kangsabanik, D. Singh, R. Venkatesh, P. Babu, K. Suresh and A. Alam, *Physical Review B*, 2021, **104**, 134406.
33 M. Mukadam, S. Roy, S. Meena, P. Bhatt and S. Yusuf, *Physical Review B*, 2016, **94**, 214423.
34 G. Pourebrahim, F. Ahmadian and P. Momeni, *Journal of Superconductivity and Novel Magnetism*, 2019, **32**, 3305–3314.
35 T. T. Hoang, S. Rhim and S. Hong, *Physical Review Materials*, 2022, **6**, 055001.
36 G. Wang, C. Li, J. Feng, Z. Zhang, X. Yuan, Y. Liu, S. Song, J. Liu, D. Wang, Z. Lu *et al.*, *Journal of Alloys and Compounds*, 2022, **891**, 161856.
37 M. Singh, H. S. Saini, J. Thakur, A. H. Reshak and M. K. Kashyap, *Journal of alloys and compounds*, 2013, **580**, 201–204.
38 S.-Y. Lin, X.-B. Yang and Y.-J. Zhao, *Journal of magnetism and magnetic materials*, 2014, **350**, 119–123.
39 S. Berri, M. Ibrir, D. Maouche and M. Attallah, *Computational Condensed Matter*, 2014, **1**, 26–31.
40 M. Avdeev and J. R. Hester, *Journal of Applied Crystallography*, 2018, **51**, 1597–1604.
41 J. Rodríguez-Carvajal, *Physica B: Condensed Matter*, 1993, **192**, 55–69.
42 P. E. Blöchl, *Physical Review B*, 1994, **50**, 17953.
43 G. Kresse and J. Hafner, *Physical Review B*, 1993, **48**, 13115.
44 G. Kresse and J. Hafner, *Journal of Physics: Condensed Matter*, 1994, **6**, 8245.
45 B. K. Perdew, J P and M. Ernzerhof, *Physical Review Letters*, 1996, **77**, 3865.

46 I. Galanakis, P. Dederichs and N. Papanikolaou, *Physical Review B*, 2002, **66**, 174429.

47 I. Galanakis, P. Mavropoulos and P. H. Dederichs, *Journal of Physics D: Applied Physics*, 2006, **39**, 765.

48 K. Özdoğan, E. Şaşıoğlu and I. Galanakis, *Journal of Applied Physics*, 2013, **113**, 193903.

49 B. Balke, S. Wurmehl, G. H. Fecher, C. Felser, M. C. Alves, F. Bernardi and J. Morais, *Applied physics letters*, 2007, **90**, 172501.

50 L. Bainsla, A. Yadav, Y. Venkateswara, S. Jha, D. Bhattacharyya and K. Suresh, *Journal of Alloys and Compounds*, 2015, **651**, 509–513.

51 B. Ravel, M. Raphael, V. Harris and Q. Huang, *Physical Review B*, 2002, **65**, 184431.

52 S. Chakraborty, S. Gupta, S. Pakhira, A. Biswas, Y. Mudryk, R. Choudhary, A. Kumar, A. Das and C. Mazumdar, *arXiv preprint arXiv:2306.14836*, 2023.

53 S. Chakraborty, S. Gupta, V. Bhasin, S. Pakhira, C. Barreteau, J.-C. Crivello, S. N. Jha, D. Bhattacharyya, M. Avdeev, V. Paul-Boncour *et al.*, *arXiv preprint arXiv:2306.14831*, 2023.

54 D. C. Koningsberger and R. Prins, 1987.

55 B. Ravel and M. Newville, *Journal of synchrotron radiation*, 2005, **12**, 537–541.

56 D. Bombor, C. G. Blum, O. Volkonskiy, S. Rodan, S. Wurmehl, C. Hess and B. Büchner, *Physical review letters*, 2013, **110**, 066601.

57 Y. Venkateswara, S. S. Samatham, A. K. Patel, P. Babu, M. R. Varma, K. Suresh and A. Alam, *Physical Review B*, 2021, **104**, 094402.

58 D. Rani, L. Bainsla, K. Suresh and A. Alam, *Journal of Magnetism and Magnetic Materials*, 2019, **492**, 165662.

59 P. A. Lee and T. Ramakrishnan, *Reviews of modern physics*, 1985, **57**, 287.

60 A. Yadav and S. Chaudhary, *Journal of Applied Physics*, 2015, **117**, 083911.

61 L. Zhu and J. Zhao, *Scientific reports*, 2017, **7**, 42931.

62 K. Srinivas, T. Prasanna Kumari, M. Manivel Raja and S. Kamat, *Journal of Applied Physics*, 2013, **114**, 033911.

63 D. Rani, J. Kangsabanik, K. Suresh, N. Patra, D. Bhattacharyya, S. Jha and A. Alam, *Physical Review Applied*, 2018, **10**, 054022.

64 E. Grüneisen, *Annalen der Physik*, 1933, **408**, 530–540.

65 N. Nagaosa, *Journal of the Physical Society of Japan*, 2006, **75**, 042001–042001.

66 K. Manna, L. Muechler, T.-H. Kao, R. Stinshoff, Y. Zhang, J. Gooth, N. Kumar, G. Kreiner, K. Koepernik, R. Car *et al.*, *Physical Review X*, 2018, **8**, 041045.

67 Y. Tian, L. Ye and X. Jin, *Physical review letters*, 2009, **103**, 087206.

68 P. Nozieres and C. Lewiner, *Journal de Physique*, 1973, **34**, 901–915.

69 N. Shahi, A. K. Jena, G. K. Shukla, V. Kumar, S. Rastogi, K. Dubey, I. Rajput, S. Baral, A. Lakhani, S.-C. Lee *et al.*, *Physical Review B*, 2022, **106**, 245137.